Lab on a Chip

PAPER

View Article Online
View Journal | View Issue

Cite this: *Lab Chip*, 2024, **24**, 3284

Electrolyte-gated amorphous IGZO transistors with extended gates for prostate-specific antigen detection†

Xuemei Yin,[a] Xingqi Ji,[a] Wenlong Liu,[a] Xiaoqian Li,[a] Mingyang Wang,[a] Qian Xin,[ab] Jiawei Zhang,[a] Zhuocheng Yan*[a] and Aimin Song *[cd]

Received 19th March 2024,
Accepted 2nd June 2024

DOI: 10.1039/d4lc00247d

rsc.li/loc

The prostate-specific antigen (PSA) test is considered an important way for preoperative diagnosis and accurate screening of prostate cancer. Current antigen detection methods, including radioimmunoassay, enzyme-linked immunosorbent assay and microfluidic electrochemical detection, feature expensive equipment, long testing time and poor stability. Here, we propose a portable biosensor composed of electrolyte-gated amorphous indium gallium zinc oxide (a-IGZO) transistors with an extended gate, which can achieve real-time, instant PSA detection at a low operating voltage (<2 V) owing to the liquid-free ionic conductive elastomer (ICE) serving as the gate dielectric. The electric double layer (EDL) capacitance in ICE enhances the accumulation of carriers in the IGZO channel, leading to strong gate modulation, which enables the IGZO transistor to have a small subthreshold swing (<0.5 V dec^{-1}) and a high on-state current (~4 × 10^{-4} A). The separate, biodegradable, and pluggable sensing pad, serving as an extended gate connected to the IGZO transistor, prevents contamination and depletion arising from direct contact with biomolecular buffers, enabling the IGZO transistor to maintain superior electronic performance for at least six months. The threshold voltage and channel current of the transistor exhibit excellent linear response to PSA molecule concentrations across five orders of magnitude ranging from 1 fg mL^{-1} to 10 pg mL^{-1}, with a detection limit of 400 ag mL^{-1} and a detection time of ~5.1 s. The fabricated biosensors offer a point-of-care system for antigen detection, attesting the feasibility of the electrolyte-gated transistors in clinical screening, healthcare diagnostics and biological management.

Introduction

Prostate-specific antigen (PSA) has been used as a serum marker for detecting prostate cancer, which not only offers great diagnostic benefits in assisting with staging and early detection but also plays an important role in preventing cancer from developing.[1,2] Although commonly used detection methods, including immunofluorescence technology, radioimmunoassay, enzyme-linked immunosorbent assay, have greatly facilitated the development of antigen detection biology,[3–5] the inherent shortcomings, such as complex operation, expensive instruments, long reaction time, and poor stability, hinder their widespread applications. Recently, biosensors based on extended-gate transistors with excellent device performance have been developed for highly sensitive detection of antigen molecule concentrations.[6–8] For instance, Lee *et al.* proposed a biosensor based on a self-amplified, extended-gate phosphorus-doped poly-Si transistor with an operating voltage range of −30 to 60 V for sensitive detection of the hepatitis B surface antigen.[9] The work indicates that with the extended-gate structure, sensing pads can be separated from the transistors to prevent solution erosion during biomodification and biosensing.[10,11] However, the high operating voltage of the transistors may damage biomolecule structures and affect biological functions, restricting improvements in sensitivity and detection limit.[12–14]

To decrease the operating voltage, it is necessary to develop new materials with improved dielectric performance for enhancing carrier modulation in extended-gate transistors. Currently, oxide dielectric materials with high dielectric constant such as alumina (Al_2O_3) and hafnium oxide (HfO_2) have been developed to achieve high-

[a] *School of Integrated Circuits, Shandong University, Jinan 250100, China. E-mail: yanzhuocheng@sdu.edu.cn*
[b] *State Key Laboratory of Crystal Materials, Institute of Novel Semiconductors, Shandong University, Jinan 250100, China*
[c] *Institute of Nanoscience and Applications, College of Engineering, Southern University of Science and Technology, Shenzhen 518055, China*
[d] *School of Electrical and Electronic Engineering, University of Manchester, Manchester M13 9PL, UK. E-mail: A.Song@manchester.ac.uk*

† Electronic supplementary information (ESI) available: Electrolyte-gated amorphous IGZO transistors with extended gates for prostate-specific antigen detection. See DOI: https://doi.org/10.1039/d4lc00247d

speed and low-voltage electronic devices with decreased leakage current and power consumption.[15,16] Lee *et al.* reported that zinc oxide (ZnO) transistors with HfO_x gate insulator achieved an operating voltage less than 20 V *via* atomic-layer-deposition for nonvolatile memory and artificial synapse in neuromorphic systems.[17–19] Liang *et al.* used fully inkjet-printed method to obtain high-quality indium tin oxide (ITO)-based thin film transistors and logic inverters with Al_2O_3 as dielectric layer, showing a notably high gain of 181 at a low-supply voltage of 3 V.[20] Although the extended-gate transistors with high-κ dielectric exhibit high charge storage capacity and high driving current at low operating voltage, the process requires high-temperature synthesis and expensive vacuum equipment, which increases the cost and complexity.[21] To this end, ionic liquid electrolytes featuring relatively high capacitance and excellent electrochemical stability have been developed to replace the high-κ dielectric layers in extended-gate transistors, in which anions and cations migrate towards different electrodes under an electric field, thereby forming tightly packed electric double layers (EDLs) at the electrolyte/semiconductor and gate-electrode/electrolyte interfaces.[22–24] Wang *et al.* reported gas sensors based on a mixed ionic liquid electrolyte-gated IGZO transistor exhibiting a low working temperature, high detection sensitivity, fast response and recovery times.[25] Shaji *et al.* proposed a ZnO synaptic transistor with imidazolium-based ionic liquid serving as the gate dielectric, which demonstrated improved saturation mobility and biological synaptic functions under drain voltage <0.3 V.[26]

Despite of the double layer capacitance capable of effectively modulating the channel carriers in extended-gate transistors, ionic liquid electrolytes exhibit poor stability due to solvent volatility and leakage, as well as poor contact interface between the dynamically changing liquid electrolytes and the channel, which adversely affect the electronic performance of transistors, especially during long-term operation.[27,28] For example, high reactivity of most Si compounds with water in electrolytes may cause poor stability at the electrolyte/semiconductor interface, and thereby lead to reduction in electronic performance.[29] Besides, some two-dimensional materials such as selenium disulfide are sensitive to moisture, and the possible side reactions when contacted with electrolytes hinder the practical applications in electrolyte-gated transistors.[30] Thus, developing a dielectric layer with excellent stability and a high dielectric constant that can achieve stable interfacial contact and efficient gate coupling with the semiconducting channel is essential for extended-gate transistors to realize immediate, reliable and prolonged PSA detection at low operating voltages.

Herein, we demonstrate a disposable and point-of-care biosensor consisting of an electrolyte-gated amorphous indium gallium zinc oxide (a-IGZO) transistor and a sensing pad as extended gate, which can achieve prompt and precise PSA detection at a low operating voltage (<2 V). The EDL capacitance at the electrolyte/semiconductor and gate electrode/electrolyte interfaces within ionic conductive elastomer (ICE) enhances the accumulation of carriers in the IGZO channel, enabling the IGZO transistors with a small subthreshold swing (<0.5 V dec^{-1}) and a high on-state current ($\sim 4 \times 10^{-4}$ A). Pluggable and biologically-functionalized sensing pads allow the IGZO transistors to maintain superior electronic performance for six months by preventing IGZO channels from direct contact with biological buffers and biomolecules to minimize contamination and degradation. The threshold voltage and channel current of the transistors exhibit excellent linear response to PSA molecule concentrations across five orders of magnitude ranging from 1 fg mL^{-1} to 10 pg mL^{-1}, with a detection limit of 400 ag mL^{-1} and a detection time of $\sim$5.1 s. Our research offers critical insight into the detection of PSA molecules, and defines a rational strategy for the design and fabrication of a reusable and portable biochemical device for early screening and preoperative diagnosis of prostate cancer.

Materials and methods

Fabrication of IGZO transistors

The portable biosensor that can achieve real-time and instant PSA detection is composed of an electrolyte-gated amorphous IGZO transistor array and an extended sensing pad, as demonstrated in Fig. 1. The fabrication of IGZO transistors begins with the preparation of ICE precursor solution. First, according to the previous reported method,[31] 2 g of lithium bis(trifluoromethane)sulfonimide (LiTFSI) powder is dissolved in a solution containing 10 mL of ethylene glycol methyl ether acrylate (MEA) and 4 mL of isobornyl acrylate (IBA) at room temperature, followed by addition of 1% (v/v) polyethylene (glycol) diacrylate (PEGDA, MW $\sim$700) as crosslinker and 1% (v/v) phenylphosphinate (TPO-L) as photo-initiator. Subsequently, the solution is sonicated for 30 min and then centrifuged at 2500 rpm for 3 min to remove air bubbles so that the ICE precursor solution is obtained. After that, a layer of ICE is spin coated onto a p^{++}-Si substrate at 3000 rpm for 60 s to form the gate dielectric. After UV curing for 3 min, a 25 nm-thick a-IGZO thin film is deposited on the ICE layer *via* magnetic sputtering in a pure Ar atmosphere at 90 W with a pressure of 4.2 mTorr.[32] Next, Ti electrodes (100 nm thick) with the designed pattern are defined on the substrate using e-beam evaporation and shadow mask techniques. Finally, post-thermal annealing is conducted at 100 °C for 1 h in air to decrease the channel electron density by increasing oxygen content, thus stabilizing the electrical characteristics of the IGZO transistors.[33]

Fabrication and surface modification of sensing pads

Fig. 1b illustrates the fabrication process of the separated sensing pad, which is achieved using e-beam evaporation and micro-/nanotechnologies. Two Ti/Au electrodes (20 nm-

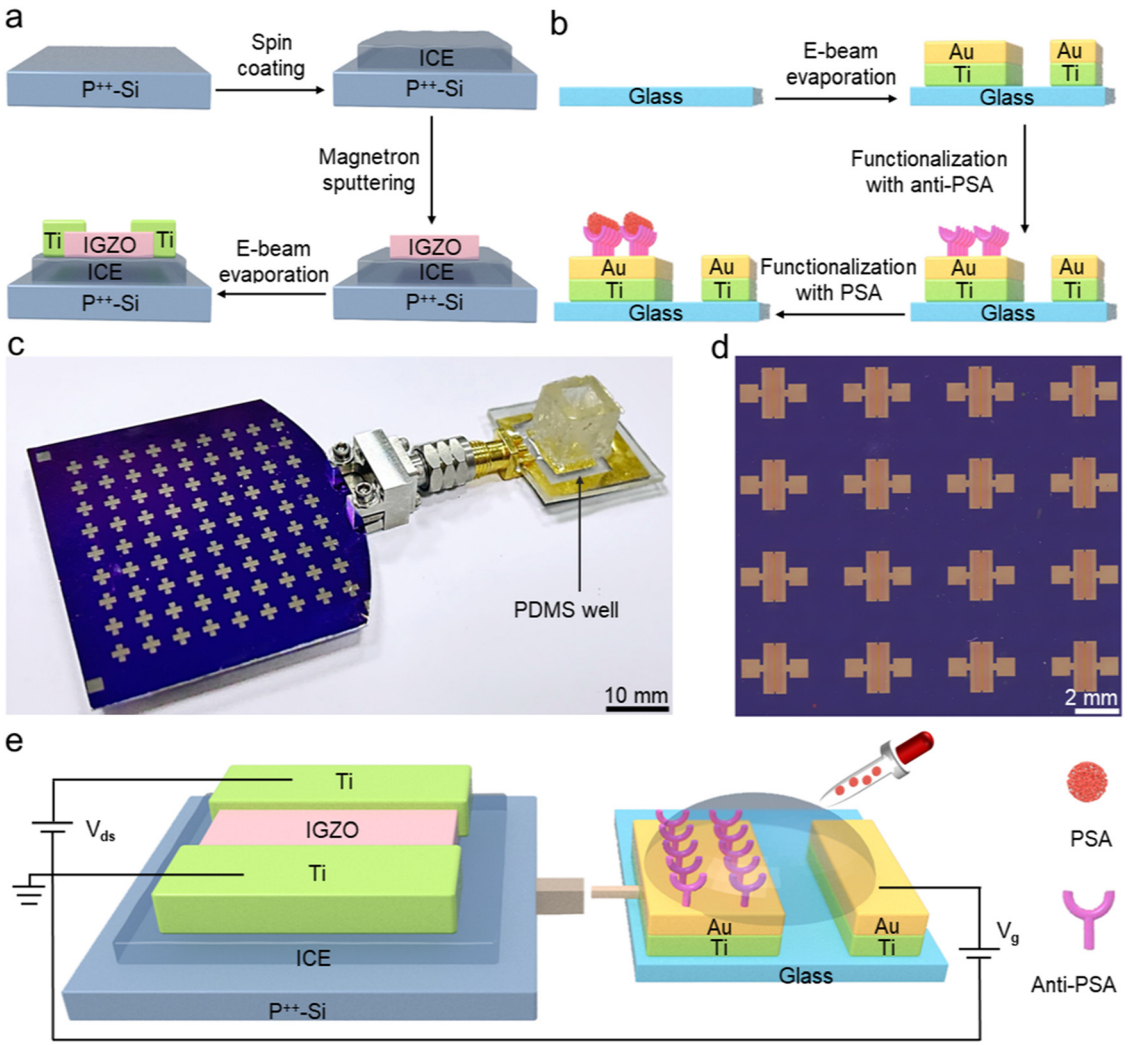

Fig. 1 Construction of IGZO transistor-based biosensor for PSA detection. Schematic illustration of fabrication process of (a) electrolyte-gated IGZO transistor and (b) extended sensing pad. (c) Optical image of electrolyte-gated IGZO transistor and extended sensing pad. (d) Microscope image of 4 × 4 IGZO transistor array. (e) Schematic diagram illustrating working mechanism and circuit connection of IGZO transistor-based biosensor.

thick layer of Ti followed by a 30 nm-thick layer of Au) with a 1.0 mm spacing are evaporated on a 15 × 15 mm^2 quartz glass substrate. Then the substrate is immersed in a 10 mM solution of 3-mercaptopropionic acid (3MPA) for 24 h at room temperature, which can introduce the carboxyl groups onto the surface through Au–S bonding. After that, the carboxylate activation solution, containing 50 mM *N*-hydroxysuccinimide (NHS) and 20 mM 1-(3-dimethylaminopropyl)-3-ethylcarbodiimide hydrochloride (EDC), is added to the 3MPA solution and reacted for 30 min to activate the carboxyl groups. Next we take out the substrate from the solution and drop the monoclonal antibody to total PSA (anti-PSA) (10 μg mL^{-1}) on its surface, and incubate it in a chamber at 4 °C for 6 h, which can be employed as specific sites to capture PSA targets.[34] Finally, the 6 × 6 mm square polydimethylsiloxane (PDMS) well is built on the sensing pad to hold the PSA solutions of volume 20 μL.

Assembly of IGZO transistor-based biosensors

After completing the fabrication of IGZO transistors and extended sensing pad, the Au electrodes on the sensing pad are designed to connect to the p^{++}-Si layer of the IGZO transistor through a pluggable interface, as illustrated in Fig. 1c. Fig. 1d exhibits the optical image of the IGZO transistor array. It can be seen that the channel width and length are 2000 μm and 60 μm, respectively. The electrical characteristics of the IGZO transistors can be measured using a Keysight B2902A precision source/measure unit after completing the circuit connection. Once the PSA droplet drips into the PDMS well, voltage is applied to the gate electrodes (Au electrodes of the sensing pad) to generate an electrical field, which controls the current flow through the channel between the drain and source (Fig. 1e). The formation of negatively charged PSA antigen–antibody complexes alters the drain-source voltage (V_{ds}), thereby

leading to a change of drain-source current (I_{ds}) and a rightward shift in the transfer curve of the IGZO transistors.

Results and discussion

Material characteristics of IGZO and ICE thin films

The optical properties of the IGZO thin film are measured using a UV-visible spectrophotometer (TU-1901). As demonstrated in Fig. 2a, the results of transmission spectra not only exhibit the high transmittance of the obtained IGZO thin film in the range of 400 to 800 nm but also reveal its semiconducting properties through the calculation of the optical band gap (E_g). By fitting the linear region of the plot of $(\alpha h\nu)^2$ *versus* $h\nu$, where α is the absorption coefficient and $h\nu$ is the photon energy, the calculated E_g is approximately 3.53 eV (Fig. 2b), which is close to the value of IGZO thin films reported in previous studies.[35] The X-ray diffraction (XRD) patterns in Fig. 2c illustrate that apart from the diffraction peaks generated by the Si substrate, there are no additional diffraction peaks, indicating the amorphous nature of the IGZO film.

We also carried out material characterization of ICE thin films. Chemical composition and functional groups are characterized using Fourier transform infrared spectroscopy (FTIR, Thermo Scientific Nicolet iS20) (Fig. 2d). The results show that there is O–H stretching vibration at 3200 cm^{-1}, asymmetric telescopic vibration at 1600 cm^{-1}, symmetric telescopic vibration of carboxylate group at 1411 cm^{-1}, and C–O telescopic vibration at 1080 cm^{-1}, demonstrating the presence of carboxyl and hydroxyl groups in ICE thin film. The oxygen-containing groups can provide conducting pathways for ions, thus imparting ionic conductivity to ICE thin films. The E_g of the ICE film is about 5.42 eV (Fig. 2e) (ESI† Fig. S1a), which is comparable with those of commonly used electrolyte dielectric materials.[36] Stylus profiler (Bruker, DektakXT) measurement shows a homogeneous ICE thin film (Fig. S1b†) with a mean film thickness about 2.5 μm. The atomic force microscopy (AFM, Benyuan CSPM5500) images in Fig. 2f and S1c† demonstrate that the root-mean-square (RMS) surface roughness of the ICE and IGZO films is 5.1 and 6.1 nm in a 10 × 10 μm^2 scanning area, respectively, indicating fairly smooth and uniform films. Overall, the material properties of IGZO and ICE thin films make them ideal choices for semiconductor layer and gate dielectric in electrolyte-gated IGZO transistors, respectively.

Capacitive properties of ITO/ICE/Ti structure

An EDL capacitor based on an ITO/ICE/Ti structure is built to investigate the capacitive properties of the ICE thin film (Fig. 3a). When a voltage is applied to the capacitor, cations (Li^+) migrate toward the negatively biased electrode, and polyanions ($TFSI^-$) approach the positively biased electrode, forming two distinct EDLs.[37] The ionic conductivity of ICE film is calculated using the equation $\sigma = L/(AR_0)$, where L represents the thickness of the ICE film, A is the cross-sectional area, and R_0 denotes the bulk resistance. The bulk resistance of the ICE film, as determined from the Nyquist plot of the impedance spectrum, is measured to be 2426 Ω using a CH 660 electrochemical analyzer (Fig. 3b). The calculated ionic conductivity of ICE is 0.046 mS cm^{-1}. The inset in Fig. 3b shows the equivalent circuit of the ICE

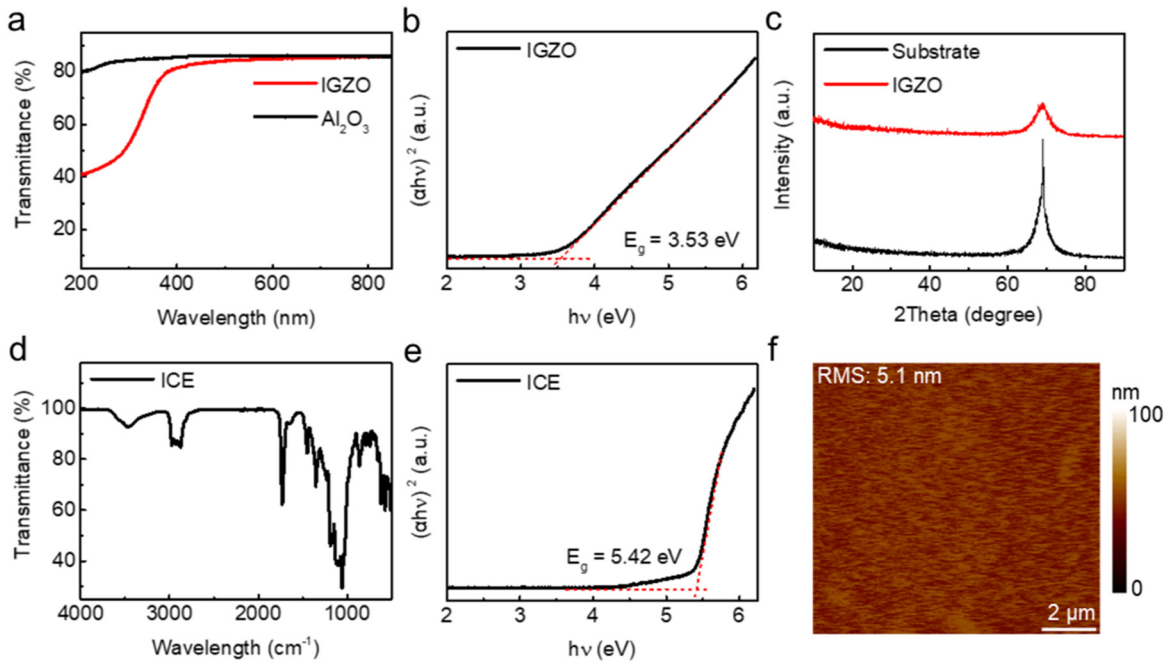

Fig. 2 Fundamental characterization of the IGZO and ICE thin film. (a) UV-visible transmittance of the sapphire (Al_2O_3) and IGZO film. (b) Fitted E_g of the IGZO film. (c) XRD of the Si substrate and the IGZO film. (d) Fitted E_g, (e) FTIR spectrum, and (f) AFM image of the ICE film.

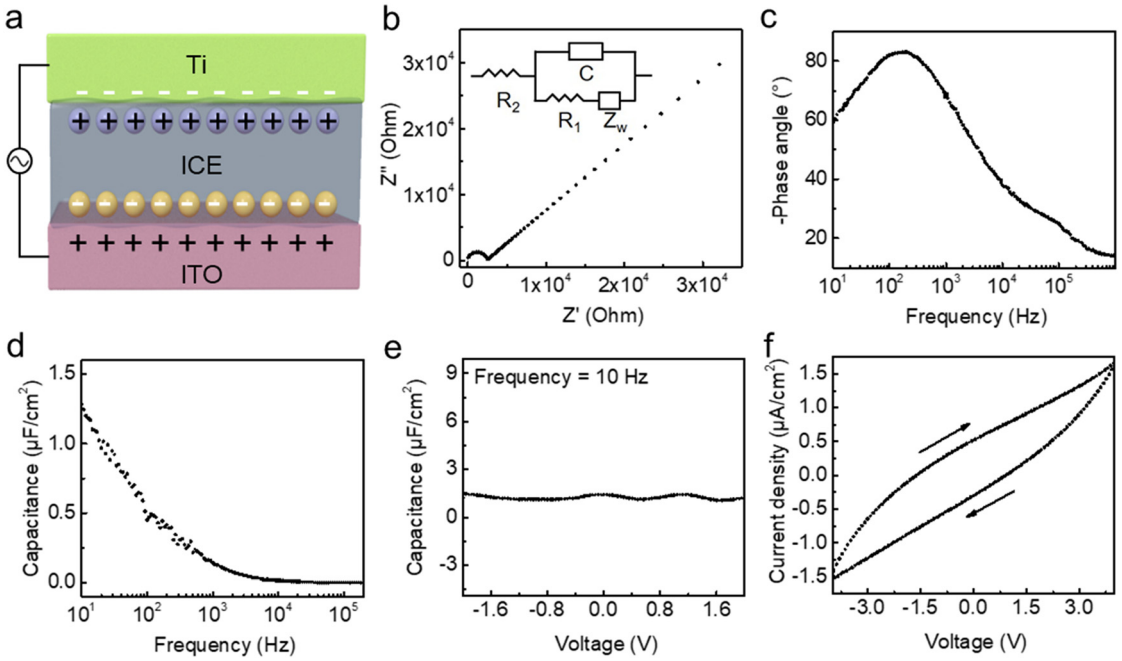

Fig. 3 Electrical performance of the ICE EDL-based capacitor. (a) Schematic illustration of the EDL capacitor. (b) Nyquist plot of the ICE film (with an inset representing the equivalent electrical circuits). (c) Phase angle-frequency characteristic, (d) capacitance–frequency, (e) capacitance–voltage, and (f) current density curve of the EDL capacitor.

capacitor, where the capacitance (C) is in parallel with a tandem resistor-Warburg impedance (R_1 – Z_W) element, and these are then connected in series with R_2 to form the fitted circuit. C represents the EDL capacitance, Z_W is the resistive contribution of ion diffusion that occurs due to the formation of the EDL, R_1 represents a tiny connected resistance factor, and R_2 denotes the resistance provided by the bulk ionic liquid. The dependence of phase angle on the frequency under an AC voltage of 0.01 V is measured to evaluate the capacitive behavior of the ICE capacitor (Fig. 3c). At high frequencies ($>10^3$ Hz), the phase angle is below −45°, demonstrating the dominant resistive nature of the ITO/ICE/Ti capacitor. As the frequency decreases from 10^3 to 10 Hz, capacitive behavior becomes evident, and the phase angle of approximately −60° at 10 Hz indicates that the generated ions accumulate near the electrolyte/electrode interface, forming a large EDL capacitance. To further explain the capacitance variation trend of the ICE capacitor, frequency-dependent capacitance is estimated. As demonstrated in Fig. 3d, the unit-area capacitance decreases from 1.3 μF cm^{-2} to 0.7 nF cm^{-2} as the frequency increases from 10 to 10^6 Hz. This decrease in capacitance with increasing frequency is attributed to the slower ion transport caused by poor chain segment motion within the ICE thin film.[38] Fig. 3e illustrates the fluctuation of the capacitance as a function of voltage at a frequency of 10 Hz. Within the working window from −2.0 to 2.0 V, the capacitance of the ICE is practically constant at approximately 1.3 μF cm^{-2}. The polymer matrix used to synthesize the ICE is hydrophobic, ensuring a good humidity stability. Fig. S2† shows the capacitance hardly changing with various humidity from 30 to 50%, indicating a desirable humidity stability. Fig. 3f shows the current density characteristics of the ICE capacitor. We can see that the ICE dielectric has a leakage current from -1.5×10^{-6} to 1.6×10^{-6} A cm^{-2} when the voltage is varied from −4.0 to 4.0 V.

Electronic performance of IGZO transistors

The schematic diagrams in Fig. 4a and b illustrate the ion migration within the ICE of IGZO transistors. The ICE film contains mobile Li^+ cations and $TFSI^-$ anions, which are uniformly distributed throughout the electrolyte in electrostatic mode (Fig. 4a). When a forward voltage ($V_g > V_{th} > 0$) is applied to the gate, as demonstrated in Fig. 4b, the $TFSI^-$ anions migrate to the gate/ICE dielectric interface under the electric field to form the first EDL. Simultaneously, Li^+ cations accumulate near the ICE dielectric/channel interface, inducing additional electrons in the IGZO active layer and thereby achieving high carrier mobility in IGZO transistors.

The influence of varying IGZO thicknesses (10, 15, 20, 25, and 30 nm) on the performance of the IGZO transistors is illustrated in Fig. 4c. The carrier concentration increases with the growth of IGZO thickness, generating more free charges to form a conductive channel at a lower gate voltage. Consequently, the drain current increases, and the threshold voltage (V_{th}) shifts in negative direction (where V_{th} is defined as the value of V_g when the I_{ds} reaches 1 μA). The IGZO transistors with the semiconducting layer of 25 nm exhibit a high switching ratio (I_{on}/I_{off}) exceeding 7.0×10^5, a high mobility (μ) of 7.4 cm^2 (V^{-1} s^{-1}), and a subthreshold swing (SS) of 0.36 V dec^{-1}. The specific characteristic parameters of

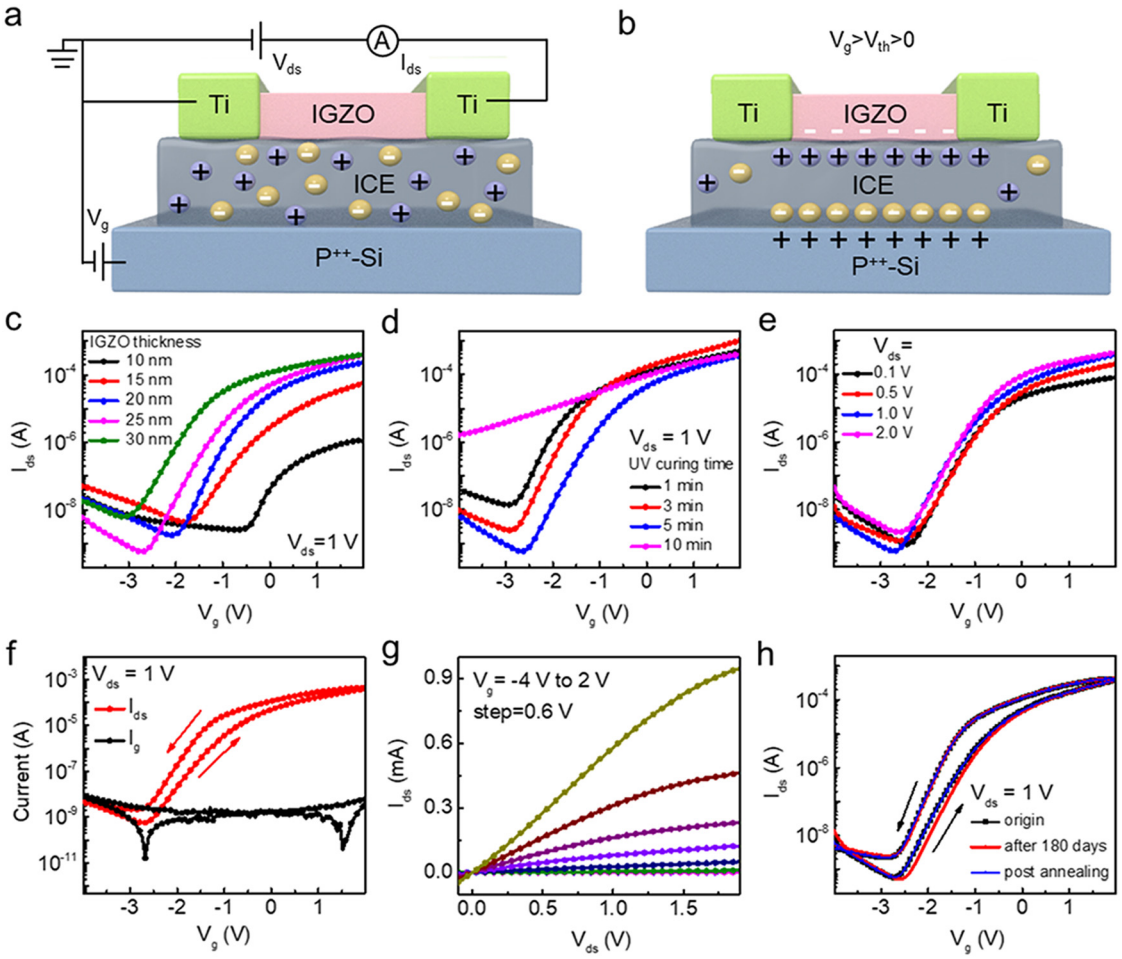

Fig. 4 Electrical properties of the IGZO transistors. Schematic cross-section structure of the IGZO transistor (a) without and (b) with the applied gate voltage. Transfer characteristics with (c) different IGZO thicknesses, (d) varying UV curing time, and (e) different values of V_{ds}. (f) Transfer and (g) output characteristics of the IGZO transistors with a 25 nm IGZO film and 5 min UV curing. (h) Stability of the IGZO transistors.

IGZO transistors with different IGZO thicknesses are listed in Fig. S3.† We can see that the transistors with IGZO thickness of 25 nm exhibit excellent device performance, which is suitable for the subsequent antigen detection. Fig. 4d shows the effect of ICE curing time on the IGZO transistors. The characteristic parameters of IGZO transistors with different curing time are listed in Fig. S4.† As the curing time increases from 1 to 5 min, the off-state current (I_{off}) decreases from 1.4 × 10^{-8} to 5.6 × 10^{-10} A, and the transfer characteristic curves shift in a positive direction, resulting in an increase of V_{th} from −2.2 to −1.2 V. The increased ICE curing time leads to a greater influx of Li^+ ions into the IGZO/ICE interface, resulting in an increased electron carrier density in the IGZO channel. When the curing time extends to 10 min, a negative shift in the threshold voltage can be observed, due to the fact that the ICE becomes almost completely solid hindering ionic transport. Thus, the ICE thin film with a curing time of 5 min is chosen as the ideal dielectric layer for the IGZO transistors. Fig. 4e shows the impact of various V_{ds} on IGZO transistors. The corresponding electrical parameters of the IGZO transistors with different value of V_{ds} are listed in Fig. S5.† The applied V_{ds} induces the motion of channel carriers resulting in the generation of I_{ds}. It is observed that I_{ds} increases proportionally with V_{ds}, and the IGZO transistor exhibits the lowest I_{off} and highest on-state current (I_{on}) when V_{ds} is set to 1 V.

In electrolyte-gated electronic transistors, the slow relaxation of ions from the formed EDLs exhibits a hysteresis characteristic. Fig. 4f demonstrates a counterclockwise hysteresis of 0.54 V in double-sweep curve of the IGZO transistors. The gate leakage current (I_g) is measured at 10 nA, a value close to the I_{off} of the IGZO transistors, indicating that the performance of the electrolyzed-gated IGZO transistors is minimally affected by the gate leakage. The output characteristic curves are used to illustrate the operating state of the transistors. As Fig. 4g shown, a linear dependence of I_{ds} on V_{ds} in the low V_{ds} region ($V_{ds} \approx 0$) demonstrates excellent ohmic contact between the Ti electrodes and the IGZO channel. As V_{ds} increases, the emergence of a saturation characteristic indicates that the IGZO transistors maintain the inherent properties of traditional n-type transistors with the ICE film serving as the

gate dielectric. The stability of the IGZO transistors as a crucial parameter is investigated because it significantly affects the electrical performance of the extended transistors. The transfer characteristics of the IGZO transistors can be maintained after 180 days (Fig. 4h). The slightly increased hysteresis may be attributed to a greater number of traps arising from prolonged exposure of the IGZO active layers to air. The hysteresis can be completely removed *via* post annealing, indicating a strong stability of the IGZO transistors.

PSA detection based on IGZO transistor-based biosensors

To estimate the feasibility of IGZO transistor-based biosensors for PSA detection, AFM images and X-ray photoelectron spectroscopy (XPS, Thermo ESCALAB 250Xi) measurements are used to study the immobilization of biomolecules on the extended pluggable sensing pad. Fig. 5a illustrates the 3D morphology and surface roughness of the sensing pad before and after functionalization with biomolecules. The Au film, deposited on a quartz glass substrate, has an RMS surface roughness of 1.2 nm, which decreases to 0.5 nm following the assembly of single molecules with 3MPA. This decrease may be attributed to the loading of organic molecules causing an improved flatness of the Au film. After modification with anti-PSA and PSA molecules, the sensing pad experiences significant increases in RMS surface roughness, reaching 4.5 nm for anti-PSA and 5.8 nm for PSA molecules. The peak-like bumps observed in the 3D morphologies further indicate the successful immobilization of anti-PSA and PSA molecules on the surface of the sensing pad. Additionally, XPS analysis is conducted to further confirm the functionalization with anti-PSA. The presence of the N element in the full XPS survey (Fig. 5b) and the sharper peak corresponding to the N–H bond in the high-resolution N 1s spectrum (Fig. 5c) indicate the introduction of the imino group onto the sensing pad, demonstrating the successful modification with anti-PSA molecules.

When the PSA molecules are added to the sensing pad, they diffuse quickly through the buffer solution. The anti-PSA on the sensing pad surface can precisely localize the PSA targets due to their high affinity and specificity (Fig. S6†).[39] The sensing response can be determined by observing the time that it takes for the signal to change.[40] To evaluate the response speed of the IGZO transistor-based biosensor for PSA detection, the channel current is continuously monitored over time without applying any gate voltage. When a 100 fg mL^{-1} PSA solution is dropped onto the sensing pad, the real-time sensing response in Fig. 6a shows a drop in current that can be attributed to antigen diffusion and specific antigen–antibody binding in the immunoassays. The channel current decrease reaches an equilibrium after approximately 5.1 s. To study the reaction time more thoroughly, we perform tests for different PSA concentrations. Fig. S7a† demonstrates responses when PSA molecules, ranging from 1 fg mL^{-1} to 10 pg mL^{-1}, are introduced into the sensing pad. For each concentration, the current stabilizes within about 5–6 s as shown in Fig. S7b–f.† This response time of 5.1 s for PSA detection is significantly shorter than the several hours or even a day required by common techniques such as radioimmunoassay, enzyme-linked immunoassay, and chemiluminescence immunoassay,[41,42] suggesting the proposed biosensor's superior response speed to PSA

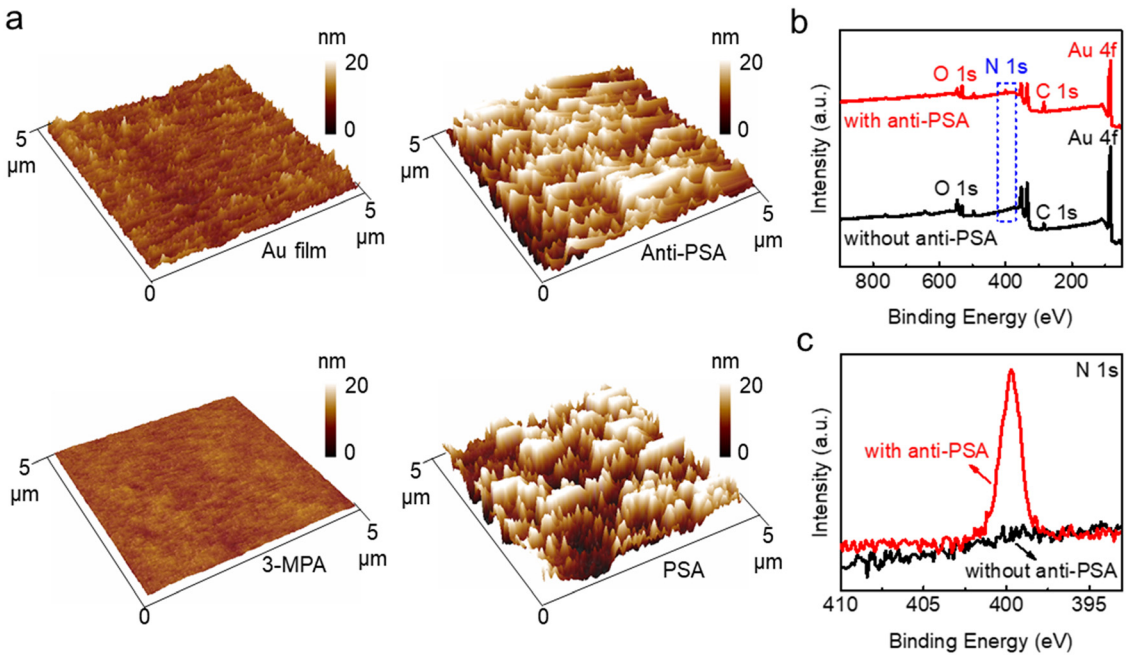

Fig. 5 Characterization of the sensing pad with different modifications. (a) AFM images showing the sensing pad modified with different molecules. (b) Full XPS survey, and (c) high-resolution spectrum of N 1s before (black line) and after (red line) functionalization of anti-PSA.

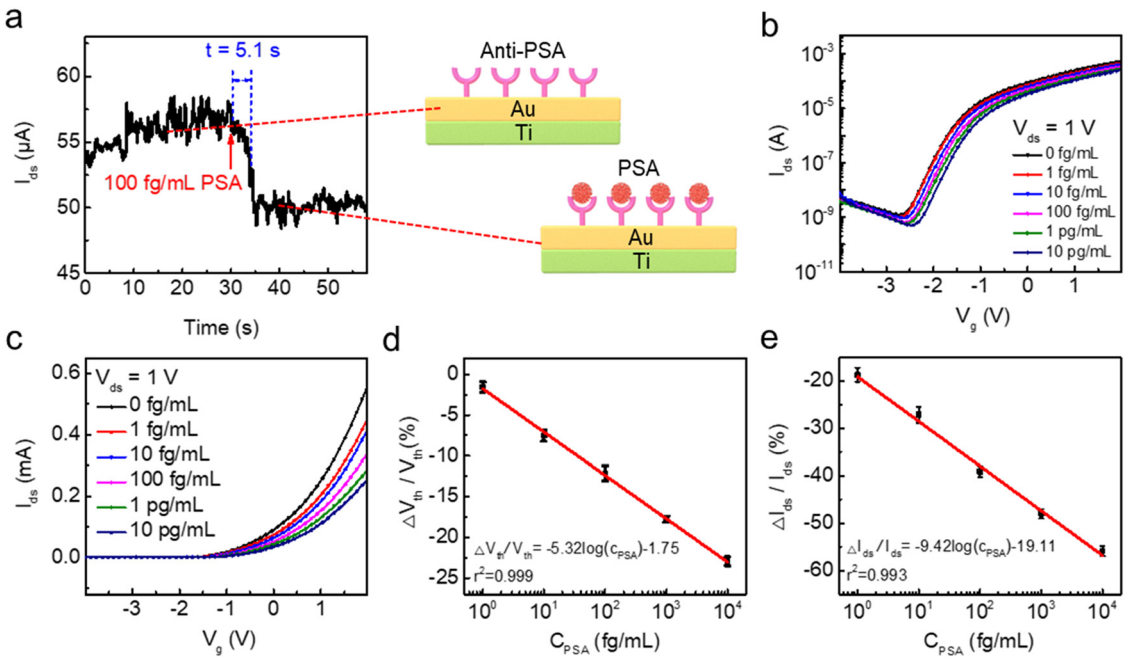

Fig. 6 Analytical performance for PSA of IGZO transistor-based biosensors for PSA detection. (a) Current change curve before and after the addition of PSA. (b) V_{th} changes at different PSA concentration (from 0 to 10 pg mL^{-1}, with V_{th} of 1.704, −1.678, −1.576, −1.497, −1.401, −1.313 V). (c) I_{ds} changes at different PSA concentration (from 0 to 10 pg mL^{-1}, with I_{ds} of 0.259, 0.210, 0.189, 0.157, 0.135, 0.114 mA). Linear relationship of (d) V_{th} and (e) I_{ds} to the PSA concentrations in the IGZO transistor-based biosensors.

detection. When the input gate potential is applied to the extended sensing pad, the negatively charged PSA antigen–antibody bindings move directionally under the influence of the electric field. The capacitance of the sensing pad (C_s) resulting from PSA and anti-PSA binding is in series with the EDL capacitance of the IGZO transistor (C_d). The V_{ds} is determined by the following equation:

$$V_{ds} = \frac{C_s}{C_s + C_d} V_g$$

The C_d is constant, and the C_s is variable with PSA concentration. The interaction between anti-PSA and different PSA targets alters V_{ds}, leading to a change of I_{ds} and a rightward shift in the transfer curve of the IGZO transistors.

To study device-to-device variation, we measure the sensing performance of three devices at different PSA concentrations. The transfer characteristics are shown in Fig. 6b and c and S8.† For three different devices, the transfer curves uniformly shift rightward, and the channel currents reduce accordingly as the PSA concentration increases from 1 fg mL^{-1} to 10 pg mL^{-1}. The specific parameters for device-to-device variation are illustrated in Table S1.† Fig. 6d demonstrates a linear relationship between the shift in threshold voltage and PSA concentrations ($\Delta V_{th}/V_{th} = -5.32 \log(C_{PSA}) - 1.75$, with a correlation coefficient r^2 of 0.999). A ten-fold increase in PSA concentrations results in an alteration of threshold voltage by more than 5%. Fig. 6e demonstrates a linear relationship between $\Delta I_{ds}/I_d$ and C_{PSA}, which can be given by: $\Delta I_{ds}/I_{ds} = -9.42 \log(C_{PSA}) - 19.11$ (where I_{ds} represents the current value when V_g is 1 V). Furthermore, compared to previous methods for measuring PSA levels, the biosensor developed in this work exhibits superior or comparable performance in terms of the linear range and detection limit, as shown in Table 1.

Table 1 Comparison of as-present work with transistor-based biosensors for the PSA detection

Device	Linear range	Detection limit	Ref.
MoS_2 transistor	100 fg mL^{-1}–10 ng mL^{-1}	800 fg mL^{-1}	43
AlGaN/GaN transistor	1 fg mL^{-1}–1 pg mL^{-1}	1 fg mL^{-1}	44
Graphene transistor	1 pg mL^{-1}–4 ng mL^{-1}	1 pg mL^{-1}	45
ZnO transistor	60 ag mL^{-1}–1 pg mL^{-1}	60 ag mL^{-1}	46
MoS_2 transistor	1 fg mL^{-1}–100 ng mL^{-1}	1 fg mL^{-1}	47
AlGaAs/GaAs transistor	5 fg mL^{-1}–5 ng mL^{-1}	5 fg mL^{-1}	48
IGZO transistor	1 fg mL^{-1}–10 pg mL^{-1}	400 ag mL^{-1}	This work

Conclusions

In conclusion, a portable biosensor is developed that combines electrolyte-gated IGZO transistor array with an extended pluggable sensing pad, which enables simple and rapid measurement of PSA molecule levels. The enhanced accumulation of carriers in the IGZO channel, facilitated by the EDL capacitance in ICE, results in high gate modulation, which allows the IGZO transistor to achieve a low subthreshold swing and a high on-state current. The biodegradable, pluggable sensing pad, connected as an extended gate to the IGZO transistor, prevents contamination and enables the device to maintain superior performance for six months. The sensor achieves a desirable linear response to PSA concentrations from 1 fg mL^{-1} to 10 pg mL^{-1} with a 400 ag mL^{-1} detection limit and a ~5.1 s detection time. The sensitive and wide-range detection of PSA levels offers promising prospects for quantification and analysis of antigens, viruses and proteins. Additionally, this technique is expected to facilitate the functionalization of biomolecules on flexible substrates such as plastics, making it an excellent candidate for the development of a biodegradable and portable miniaturized integration chip.

Author contributions

Xuemei Yin: methodology, validation, formal analysis, data curation, writing – original draft. Xingqi Ji: methodology, validation, data curation. Wenlong Liu: investigation, software. Xiaoqian Li: writing – original draft, investigation, data curation. Mingyang Wang: investigation. Qian Xin: resources, writing – review & editing. Jiawei Zhang: conceptualization, resources. Zhuocheng Yan: conceptualization, writing – review & editing. Aimin Song: conceptualization, writing – review & editing, resources, funding acquisition.

Conflicts of interest

There are no conflicts to declare.

Acknowledgements

This work was financed by National Key Research and Development Program of China (2022YFB3603900 and 2022YFA1405200), National Natural Science Foundation of China (62074094), the Royal Society grants (IEC\R2\170155 and NA170415), the Key Research and Development Program of Shandong Province (2017GGX10111), and Natural Science Foundation of Shandong Province (ZR2020ZD03, ZR2022ZD05 and ZR2021QE148).

Notes and references

1 A.-K. Kissmann, J. Andersson, A. Bozdogan, V. Amann, M. Kraemer, H. Xing, H. F. Raber, D. H. Kubiczek, P. Aspermair, W. Knoll and F. Rosenau, *Nanoscale Horiz.*, 2022, **7**, 770–778.
2 A. Chakraborty, P. Dutta, A. Wakankar and C. RoyChaudhuri, *Biosens. Bioelectron.*, 2022, **12**, 100253.
3 D. Mwanza, O. Adeniyi, S. Tesfalidet, T. Nyokong and P. Mashazi, *J. Electroanal. Chem.*, 2022, **927**, 116983.
4 Y. Huang, S. Li and V. Bhethanabotla, *Biosens. Bioelectron.*, 2023, **219**, 114822.
5 N. Li, Y. Jiang, T. Lv, G. Li and F. Yang, *Biosens. Bioelectron.*, 2022, **216**, 114598.
6 T. Li, T. Xu, Z. Yao, Y. Ding, G. Liu and F. Shan, *Appl. Phys. Lett.*, 2023, **122**, 243701.
7 V. D. Wangkheirakpam, B. Bhowmick and P. D. Pukhrambam, *J. Mater. Sci.: Mater. Electron.*, 2022, **33**, 10323–10334.
8 Y.-U. Kim and W.-J. Cho, *Chemosensors*, 2022, **10**, 122–132.
9 I. K. Lee, M. Jeun, H. J. Jang, W. J. Cho and K. H. Lee, *Nanoscale*, 2015, **7**, 16789–16797.
10 Y. Zhang, C. Sun, Y. Duan, S. Cheng and W. Hu, *Nanoscale*, 2023, **15**, 16458–16465.
11 S. Keawkusonwiwat, B. Tunhoo, K. Onlaor and T. Thiwawong, *J. Electron. Mater.*, 2023, **52**, 8095–8107.
12 D. Wang, Z. Liu, J. Li, W. Tang, Y. Huang, J. Yu, L. Xu, Q. Huang, Y. Song, L. Wang, H. Jin, K. Xi, L. Feng, X. Guo, A. Nathan and H. Ma, *Flexible Printed Electron.*, 2022, **7**, 023004.
13 A. Kumar, A. K. Goyal and N. Gupta, *ECS J. Solid State Sci. Technol.*, 2020, **9**, 115022–115033.
14 S. J. Kim, J. Jung, K. W. Lee, D. H. Yoon, T. S. Jung, S. R. Dugasani, S. H. Park and H. J. Kim, *ACS Appl. Mater. Interfaces*, 2013, **5**, 10715–10720.
15 A. Kaushik, A. Vasudev, S. K. Arya, S. K. Pasha and S. Bhansali, *Biosens. Bioelectron.*, 2014, **53**, 499–512.
16 A. Singh, A. Kaushik, R. Kumar, M. Nair and S. Bhansali, *Appl. Biochem. Biotechnol.*, 2014, **174**, 1115–1126.
17 H. Lee, K. Beom, M. Kim, C. J. Kang and T. S. Yoon, *Adv. Electron. Mater.*, 2020, **6**, 115022.
18 P. Ma, L. Du, Y. Wang, R. Jiang, Q. Xin, Y. Li and A. Song, *Appl. Phys. Lett.*, 2018, **112**, 023501.
19 P. Ma, J. Sun, G. Liang, Y. Li, Q. Xin, Y. Li and A. Song, *Appl. Phys. Lett.*, 2018, **113**, 063501.
20 K. Liang, D. Li, H. Ren, M. Zhao, H. Wang, M. Ding, G. Xu, X. Zhao, S. Long, S. Zhu, P. Sheng, W. Li, X. Lin and B. Zhu, *Nano-Micro Lett.*, 2021, **13**, 164.
21 Y. M. Fu, H. Li, T. Wei, L. Huang, F. Hidayati and A. Song, *ACS Appl. Electron. Mater.*, 2022, **4**, 2933–2942.
22 C. Sun, X. Liu, Q. Jiang, X. Ye, X. Zhu and R. W. Li, *Sci. Technol. Adv. Mater.*, 2023, **24**, 2162325.
23 D. Wang, S. Zhao, R. Yin, L. Li, Z. Lou and G. Shen, *npj Flexible Electron.*, 2021, **5**, 13–28.
24 F. Torricelli, D. Z. Adrahtas, Z. Bao, M. Berggren, F. Biscarini, A. Bonfiglio, C. A. Bortolotti, C. D. Frisbie, E. Macchia, G. G. Malliaras, I. McCulloch, M. Moser, T. Q. Nguyen, R. M. Owens, A. Salleo, A. Spanu and L. Torsi, *Nat. Rev. Methods Primers*, 2021, **1**, 66–89.
25 B. Wang, A. Thukral, Z. Xie, L. Liu, X. Zhang, W. Huang, X. Yu, C. Yu, T. J. Marks and A. Facchetti, *Nat. Commun.*, 2020, **11**, 2405.

26 M. Shaji, F. P. Jose, K. J. Saji, A. Antony and M. K. Jayaraj, *J. Mater. Sci.-Mater. El.*, 2022, **33**, 19985–19997.
27 J. Hua, M. Su, X. Sun, J. Li, Y. Sun, H. Qiu, Y. Shi and L. Pan, *Biosensors*, 2023, **13**, 696–723.
28 Y. He, Y. Yang, S. Nie, R. Liu and Q. Wan, *J. Mater. Chem. C*, 2018, **6**, 5336–5352.
29 Y. Nishimura, Y. Fukunaka, T. Nohira and R. Hagiwara, *ECS Trans.*, 2008, **11**, 13.
30 W. Lv, B. Wang, W. Lv, S. Cao, X. Luo, W. Shi, B. Zhang, Z. Wei and Z. Zeng, *Mater. Res. Express*, 2019, **6**, 12543–12550.
31 B. Yiming, Y. Han, Z. Han, X. Zhang, Y. Li, W. Lian, M. Zhang, J. Yin, T. Sun, Z. Wu, T. Li, J. Fu, Z. Jia and S. Qu, *Adv. Mater.*, 2021, **33**, e2006111.
32 J. Zhang, J. Yang, Y. Li, J. Wilson, X. Ma, Q. Xin and A. Song, *Materials*, 2017, **10**, 319.
33 X. Ji, Y. Yuan, X. Yin, S. Yan, Q. Xin and A. Song, *IEEE Trans. Electron Devices*, 2022, **69**, 6783–6788.
34 J. Yu, M. Xu, L. Liang, M. Guan, Y. Zhang, F. Yan and H. Cao, *Appl. Phys. Lett.*, 2020, **116**, 123704.
35 M. Moreira, E. Carlos, C. Dias, J. Deuermeier, M. Pereira, P. Barquinha, R. Branquinho, R. Martins and E. Fortunato, *Nanomaterials*, 2019, **9**, 1273–1286.
36 H. Shen, S. Peng, Q. Luo, J. Zhou, J. H. He, G. Zhou and X. Xu, *Adv. Funct. Mater.*, 2023, **33**, 2213820.
37 P. Zhang, W. Guo, Z. H. Guo, Y. Ma, L. Gao, Z. Cong, X. J. Zhao, L. Qiao, X. Pu and Z. L. Wang, *Adv. Mater.*, 2021, **33**, e2101396.
38 C. Luo, Y. Chen, Z. Huang, M. Fu, W. Ou, T. Huang and K. Yue, *Adv. Funct. Mater.*, 2023, **33**, 2304486.
39 H. M. Lai, Y. Tang, Z. Y. H. Lau, R. A. A. Campbell, J. C. N. Yau, C. C. Y. Chan, D. C. W. Chan, T. Y. Wong, H. K. T. Wong, L. Y. C. Yan, W. K. K. Wu, S. H. Wong, K.-W. Kwok, Y.-K. Wing, H. H. N. Lam, H.-K. Ng, T. D. Mrsic-Flogel, V. C. T. Mok, J. Y. K. Chan and H. Ko, *Nat. Methods*, 2022, **19**, 1137–1146.
40 Y. Li, Z. Peng, N. J. Holl, M. R. Hassan, J. M. Pappas, C. Wei, O. H. Izadi, Y. Wang, X. Dong, C. Wang, Y.-W. Huang, D. Kim and C. Wu, *ACS Omega*, 2021, **6**, 6643–6653.
41 P. Assari, A. A. Rafati, A. Feizollahi and R. Asadpour Joghani, *Microchim. Acta*, 2019, **186**, 484.
42 Z. Aayanifard, T. Alebrahim, M. Pourmadadi, F. Yazdian, H. S. Dinani, H. Rashedi and M. Omidi, *Eng. Life Sci.*, 2021, **21**, 739–752.
43 P. Song, P. Ou, Y. Wang, H. Yuan, S. Duan, L. Chen, H. Fu, J. Song and X. Liu, *Anal. Chim. Acta*, 2023, **1252**, 341036.
44 J. Wang, Z. Gu, X. Liu, L. Zhao, H. Peng and J. Li, *Analyst*, 2020, **145**, 2725–2730.
45 N. Mandal, V. Pakira, N. Samanta, N. Das, S. Chakraborty, B. Pramanick and C. RoyChaudhuri, *Talanta*, 2021, **222**, 121581.
46 B. Chakraborty, R. Saha, S. Chattopadhyay, D. De, R. D. Das, M. K. Mukhopadhyay, M. Palit and C. RoyChaudhuri, *Appl. Surf. Sci.*, 2021, **537**, 147895.
47 Y. Zhang, D. Feng, Y. Xu, Z. Yin, W. Dou, U. E. Habiba, C. Pan, Z. Zhang, H. Mou, H. Deng, X. Mi and N. Dai, *Appl. Surf. Sci.*, 2021, **548**, 149169.
48 J. Yu, G. Gao, B. Sun, L. Liang, Q. Shen, Y. Zhang and H. Cao, *J. Pharm. Biomed. Anal.*, 2022, **211**, 114597.